

Arteriosclerosis, Thrombosis, and Vascular Biology

JOURNAL OF THE AMERICAN HEART ASSOCIATION

American Heart
Association®



Learn and Live SM

Imaging and Quantitative Analysis of Atherosclerotic Lesions by CARS-Based Multimodal Nonlinear Optical Microscopy

Han-Wei Wang, Ingeborg M. Langohr, Michael Sturek and Ji-Xin Cheng

Arterioscler. Thromb. Vasc. Biol. 2009;29:1342-1348; originally published online Jun 11, 2009;

DOI: 10.1161/ATVBAHA.109.189316

Arteriosclerosis, Thrombosis, and Vascular Biology is published by the American Heart Association,
7272 Greenville Avenue, Dallas, TX 75214

Copyright © 2009 American Heart Association. All rights reserved. Print ISSN: 1079-5642. Online
ISSN: 1524-4636

The online version of this article, along with updated information and services, is
located on the World Wide Web at:

<http://atvb.ahajournals.org/cgi/content/full/29/9/1342>

Subscriptions: Information about subscribing to Arteriosclerosis, Thrombosis, and Vascular
Biology is online at

<http://atvb.ahajournals.org/subscriptions/>

Permissions: Permissions & Rights Desk, Lippincott Williams & Wilkins, a division of Wolters
Kluwer Health, 351 West Camden Street, Baltimore, MD 21202-2436. Phone: 410-528-4050. Fax:
410-528-8550. E-mail:

journalpermissions@lww.com

Reprints: Information about reprints can be found online at

<http://www.lww.com/reprints>

Imaging and Quantitative Analysis of Atherosclerotic Lesions by CARS-Based Multimodal Nonlinear Optical Microscopy

Han-Wei Wang, Ingeborg M. Langohr, Michael Sturek, Ji-Xin Cheng

Objective—The purpose of this study was to assess the ability of label-free multimodal nonlinear optical (NLO) microscopy to characterize, and thus enable quantitative in situ analyses of, different atherosclerotic lesion types, according to the original scheme suggested by the AHA Committee.

Methods and Results—Iliac arteries were taken from 24 male Ossabaw pigs divided into lean control and metabolic syndrome groups and were imaged by multimodal NLO microscopy where sum-frequency generation (SFG) and 2-photon excitation fluorescence (TPEF) were integrated on a coherent anti-Stokes Raman scattering (CARS) microscope platform. Foam cells, lipid deposits, matrices, and fibrous caps were visualized with submicron 3D resolution. Starting from the adaptive intimal thickening in the initial stage to the fibrous atheroma or mineralization in the advanced stages, lesions were visualized without labels. Histological staining of each lesion confirmed the lesion stages. Lipid and collagen contents were quantitatively analyzed based on the CARS and SFG signals. Lipid accumulation in thickened intima culminated in type IV whereas the highest collagen deposition was found in Type V lesions. Luminal CARS imaging showed the capability of viewing the location of superficial foam cells that indicate relatively active locus in a lesion artery.

Conclusions—We have demonstrated the capability of CARS-based multimodal NLO microscopy to interrogate different stages of lesion development with subcellular detail to permit quantitative analysis of lipid and collagen contents. (*Arterioscler Thromb Vasc Biol.* 2009;29:1342-1348.)

Key Words: coherent anti-Stokes Raman scattering ■ multimodal nonlinear optical microscopy
■ Ossabaw miniature swine ■ atherosclerosis ■ histopathology

Atherosclerosis, the major cause of cardiovascular diseases, has been a leading contributor to morbidity and mortality in the United States,¹ and it has been on the rise globally.² The statistics that account for the rise in incidence consequently call for new imaging techniques to advance the research and diagnosis of atherosclerosis. Current imaging methods, such as x-ray angiography, MRI, intravascular ultrasound (IVUS), computed tomography, and optical coherence tomography (OCT) allow exquisite delineation of advanced lesions.³ Notably, MRI can achieve molecular imaging using contrast agents.^{4,5} Also, by using spectral analysis to identify lesion components, IVUS can perform virtual histology.^{6–8} Nonetheless, these techniques have not yet reached submicron resolution. As the gold standard, histology provides high performance in biopsy studies, but it is not feasible for live tissue imaging. In addition, with technical advances, fluorescence microscopy with 1- and 2-photon excitation has been applied to vascular and atherosclerosis studies^{5,9} with the capability of identifying cellular and

molecular compositions in vivo with labeling.¹⁰ However, these techniques are subject to possible compromises to labeling, such as photobleaching, the requirement for extra incubation, or limited circulation lifetime, all of which could be less optimal for arterial studies. Thus, it is intriguing to explore label-free imaging methods which can also provide chemical selectivity and submicron resolution.

Nonlinear optical (NLO) microscopy¹¹ has become a powerful tool for imaging biological samples by its unique advantages of inherent 3D resolution, near-IR excitation for superior optical penetration,¹² and lower photodamage. By using endogenous sources of NLO signals, label-free NLO imaging of unstained tissues has been intensively studied, and several examples of label-free imaging methods have been reported. Specifically, 2-photon excited fluorescence (TPEF) microscopy has been applied to tissue imaging with intrinsic fluorescence.^{11,13} Being sensitive to noncentrosymmetric structures,¹⁴ second harmonic generation (SHG), also called frequency doubling, has been used for imaging membranes¹⁵

Received February 12, 2008; revision accepted May 28, 2009.

From the Weldon School of Biomedical Engineering (H.-W.W., J.-X.C.), the Department of Comparative Pathobiology (I.M.B.), and the Department of Chemistry (J.-X.C.), Purdue University, West Lafayette, Ind; and the Department of Cellular & Integrative Physiology (M.S.), Indiana University School of Medicine, Indianapolis.

Correspondence to Ji-Xin Cheng, 206 S Martin Jischke Drive, West Lafayette, IN 47907-2032. E-mail jcheng@purdue.edu

© 2009 American Heart Association, Inc.

Arterioscler Thromb Vasc Biol is available at <http://atvb.ahajournals.org>

DOI: 10.1161/ATVBAHA.109.189316

and protein fibrils.^{16–19} Sum frequency generation (SFG)¹⁴ derives its signal from noncentrosymmetric molecules at the sum frequency of 2 excitation sources with imaging capability similar to that of SHG for biological tissues.¹⁸ Third harmonic generation (THG) has been demonstrated for imaging of interface heterogeneities²⁰ and lipid bodies.²¹

Most notably, a third-order NLO imaging technique known as coherent antistokes Raman scattering (CARS) microscopy^{22,23} has been successfully applied to live tissue imaging with vibrational selectivity.^{24,25} To achieve such selectivity, the CARS process involves a pump laser beam at frequency ω_p and a Stokes laser beam at frequency ω_s . By tuning the beating frequency ($\omega_p - \omega_s$) to be resonant with the symmetrical CH_2 vibration, CARS shows high sensitivity and selectivity to lipid droplets²⁶ and lipid membranes.²⁷ This unique characteristic makes CARS microscopy an attractive tool for atherosclerosis studies. Before the use of CARS for vascular studies, other NLO methods have been used to visualize the arterial wall without labeling, but these were limited to viewing collagen and elastic fibril structures.^{13,28} Therefore, beyond the fibrils, cells, such as endothelial cells, smooth muscle cells, and foam cells, must be detected by TPEF with the aid of labels.^{29,30} Le et al first applied CARS to visualize lipid-laden cells in atheroma but used an additional femto-second laser for other NLO modalities.³¹ By integrating SFG and TPEF on a CARS platform and using the same picosecond laser source, multimodality was obtained with lower cost and lower photodamage potential.³² Using such a setup, it has been shown that the CARS signal from cell membranes and CH_2 -rich amino acid residues allowed the detection of arterial cells and extracellular protein fibrils in normal arteries without labeling.³²

In spite of these advances, it is still unknown whether NLO microscopy can distinguish different types of plaques. In view of the increasing incidence of atherosclerosis leading to cardiovascular disease, it is critical to address this question for developing an NLO-based endoscopy capable of distinguishing different stages of atherosclerotic disease in vivo. In the current study, we demonstrate that CARS-based multimodal NLO imaging could recognize different lesion types based on the scheme of atherosclerosis classification suggested by the American Heart Association (AHA) and modified by other authorities.^{33–36} Furthermore, we show that the multimodal approach that uses CARS and SFG signals allows quantitation of collagen and lipid contents in lesions from early to advanced stages. As described below, we have used an Ossabaw swine model that closely mimics metabolic syndrome in humans.³⁷

Materials and Methods

Tissue Specimen

Iliac arteries in the vicinity of the bifurcation of the caudal aorta were collected from 24 male Ossabaw pigs (a colony in the Comparative Medicine Program of the Purdue University and Indiana University School of Medicine, Ind.) of 2 diet groups (for details see supplemental materials, available online at <http://atvb.ahajournals.org>): healthy lean control pigs ($n=11$) and metabolic syndrome pigs ($n=13$). Arteries were rinsed with saline and preserved by zinc formalin fixation immediately after harvest. Phosphate buffered saline was used to wash the samples before imaging. The arteries were sliced horizon-

tally (≈ 1 mm in thickness) for cross-sectional NLO imaging (supplemental Figure IA and IB) and were incised longitudinally for luminal imaging. Serial slices of each artery were collected. NLO and histology images were acquired at the most affected sector according to the thickening severity, plaque and core size, or stenosis condition. The fixation process maintained the integrity of arterial structures, as validated by NLO imaging of the tissues before and after fixation.

CARS-Based Multimodal NLO Imaging

Details of our multimodal imaging setup can be found in the supplemental materials. In brief, 2 synchronized 5-ps lasers (Tsunami, Spectra-Physics) operating at 80 MHz repetition rate were parallel-polarized, collinearly combined, and directed into a laser scanning microscope (FV300/IX71, Olympus). Signals were detected by external photomultiplier tubes (PMT, Hamamatsu).

For CARS imaging, the beating frequency was tuned to 2840 cm^{-1} which matches the symmetrical CH_2 stretch vibration.^{22,24} Bandpass filters (600/65 nm, Ealing Catalog) were used to transmit the CARS signal of ≈ 588 nm. The average powers of the master and slave laser beams at the sample were 40 mW and 20 mW. The same lasers were used to produce the SFG signal of ≈ 393 nm. Two bandpass filters (HQ375/50m-2p, Chroma) were used to transmit the backward SFG signal. For TPEF imaging of nonlabeled samples, 2 bandpass filters (hp520/40m-2p, Chroma) were used to transmit auto-fluorescence. For TPEF imaging of Doxorubicin-labeled samples, 2 600/65-nm filters were used. The fluorescence was generated by only using the master laser (≈ 707 nm) to avoid the CARS signal.

Histology Analysis

Artery sections adjacent to those imaged by NLO imaging were immersion-fixed in formalin and routinely processed with paraffin embedding for histological staining.³⁸ A detailed description of staining can be found in the supplemental materials. Histology samples were blindly examined by pathologist and coauthor, Dr Ingeborg Langohr, using a Nikon Eclipse E400 microscope (Nikon Corp) equipped with air objectives and a Spot Insight Camera (Diagnostic Instrument).

Analysis of Area Percentage of Lipid and Collagen

Collagen content in the thickened intima of each lesion was calculated according to the SFG signal. By setting a signal threshold of 30 in the 8-bit (255) range, area percentage of collagen in intima was measured. Area percentage of lipid droplet content in the thickened intima was calculated according to the CARS signal. A threshold was used so that the CARS signals from cell membrane and other structures, such as elastin, were not counted (for details see the supplemental materials). Images for quantitative analysis were derived with the use of the $20\times$ air objective. The measurement was conducted at the most-affected sectors within the plaque shoulder of lesions. The ImageJ software was used for the percentage measurement. Data are presented as mean \pm SD ($P < 0.01$). One-way ANOVA was used to identify the significant difference among lesion types. $P < 0.05$ was considered significant.

Results

NLO images of the cross-sectional view of iliac arteries were analyzed and classified into different atherosclerotic lesion types according to the scheme suggested by the AHA Committee and modified by other authorities^{33–36} (supplemental Table I). The NLO images were compared with histological evaluations. Figures 1 to 5 illustrate multimodal NLO images of atherosclerosis lesions. Images of normal arteries (data not shown) and the early lesions, such as type I and II, were obtained from the 11 lean control pigs. Intermediate to advanced lesions, including types III, IV, V, and VII, were derived from the pigs of the metabolic syndrome group. Types VI and VIII were not found in the samples collected for

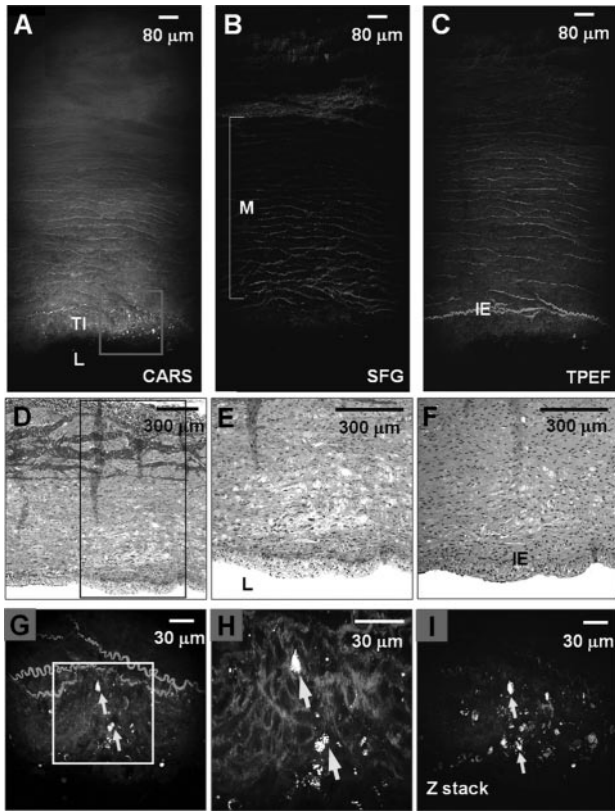


Figure 1. Representative images of a Type I lesion inspected by CARS (A), SFG (B), and TPEF (C). D and E, Masson trichrome staining. F, H&E staining. Rectangular window in D indicates the relative area of NLO images in A through C. G, Colocalized NLO image corresponding to the red square in A. Arrows indicate scattered lipid-laden cells. H, Colocalized image corresponding to the white square in G. I, Z-stack CARS image. L indicates lumen; TI, thickened intima; M, tunica media; IE, internal elastic lamina; gray for CARS; blue for SFG; green for TPEF. The same color code is used in other figures.

this study. NLO images were representatively demonstrated around the most severe portion of the eccentric plaques or partial media-intima thickening lesions.

NLO Identification of Early Atherosclerotic Lesions

Figures 1 and 2 show the representative results of early lesions. In Figure 1A through 1C, the stratification of arterial composition is similar to a normal artery except the observation of the adaptive intima thickening with scattered lipid-laden cells viewed by CARS. The adaptive thickening, ordered collagen fibrous tissues, and elastic lamella, which were imaged by CARS, SFG, and TPEF, respectively, elucidated the status of the artery as a Type I lesion. In comparison, the histology observations also showed the intimal thickening (Figure 1D through 1F) referring to the location of the internal elastic lamina (Figure 1F), which is also in keeping with the observation in Figure 1C and 1G. In addition, the histology images of collagen staining in Figure 1D and 1E highly support the SFG signal shown in Figure 1B and 1H. The scattered foam cells specifically identified by CARS³¹ (Figure 1G through 1I, arrows) further confirm the adaptive thickening milieu.^{35,36}

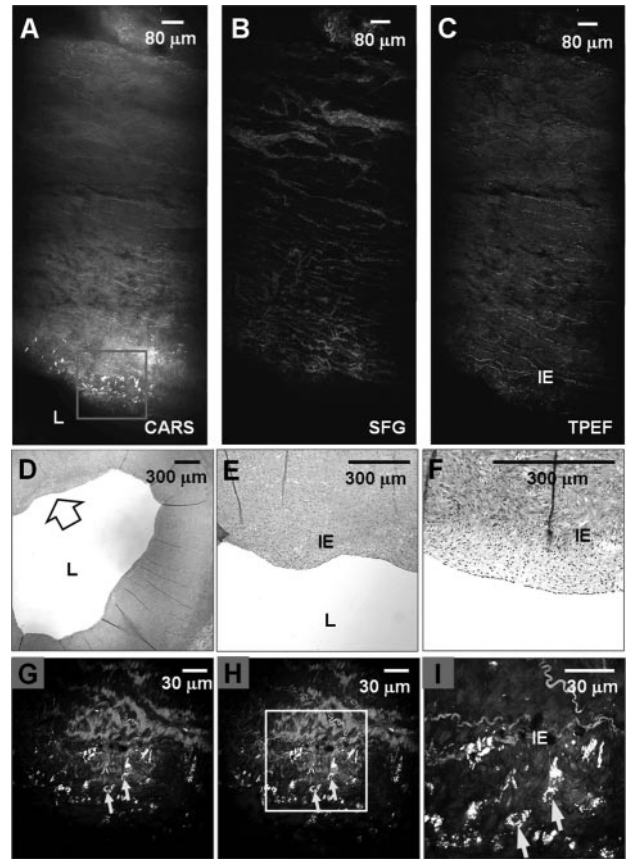


Figure 2. Representative images of a Type II lesion inspected by CARS (A), SFG (B), and TPEF (C). D and E, H&E staining. Wide arrow indicates the relative location in A through C. F, Masson trichrome staining. G and H, Colocalized NLO images from the red square in A. CARS reveals aggregated lipid-laden cells (arrows) with elongated shape (possibly smooth muscle cells) in the thickened intima. I, Colocalized image relating to the white square in H.

Figure 2A through 2C shows the NLO images of the cross-section of a typical Type II lesion. The CARS image (Figure 2A) shows a fatty streak lesion characterized by the accumulation of closely spaced foam cells around the luminal area. This observation compares favorably to the histology images in Figure 2D through 2F, which also show the thickening milieu. The bubbly and granular scenario in the thickened part, which implies lipid accumulation, agrees with the same lesion viewed in NLO imaging. Moreover, the Masson trichrome staining in Figure 2F agrees with the collagen distribution in Figure 2B and 2G. Figure 2G shows a smaller collagen deposit in the intima in the proximity of lumen. These conditions match the observation stipulating that collagen secretion is mainly attributed to modified smooth muscle cells.³⁹ Along with the foam cell accumulation (Figure 2G through 2I), the adaptive thickening is suggested to associate with pathological thickening and future lesions.⁴⁰ When CARS imaging of lipids is combined with TPEF imaging of internal elastic lamina, the results show that the foam cells resided inside the intima layer (Figure 2H). The TPEF signal around foam cells and arterial cells is likely attributed to the auto-fluorescence of oxidized-LDL⁴¹ and NAD(P)H species.⁴² Because the TPEF signal from

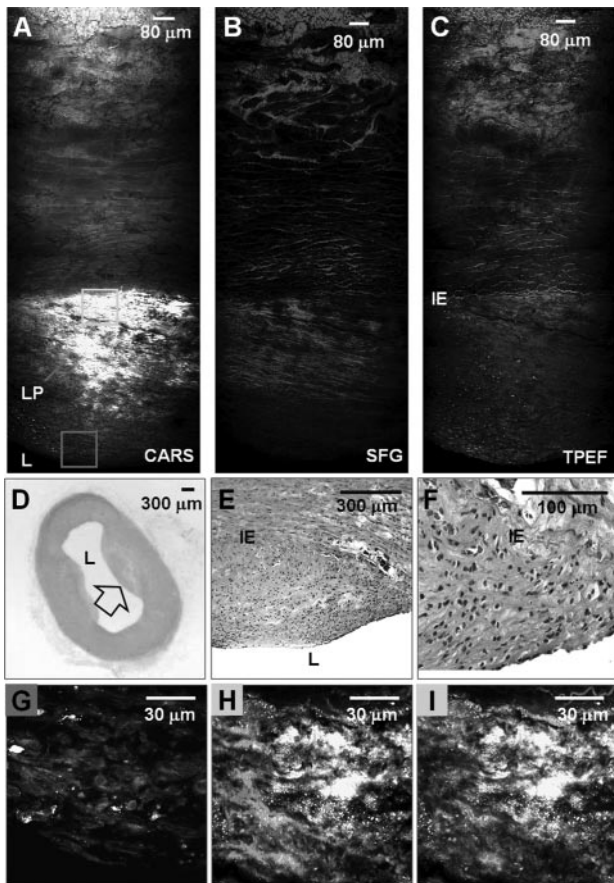


Figure 3. Representative images of a Type III lesion inspected by CARS (A), SFG (B), and TPEF (C). LP indicates lipid pools. D, Subgross image of H&E staining. Wide arrow indicates the relative location in A through C. E and F, Zoomed-in H&E around the pathological intima-media interface. G, Colocalized NLO image from the red square in A shows a cell-dominated distribution with no signal of collagen. H and I, Colocalized NLO images from the yellow square in A.

foam cells only minimally contributes to the CARS channel,³¹ the strong CARS signal from the foam cells specifically shows the distribution of granulated lipid (Figure 2I).

NLO Identification of Intermediate to Advanced Atherosclerotic Lesions

The intermediate lesion of atherosclerosis, which is defined as Type III, contains scattered lipid pools (Figure 3A) in a relatively thicker intima (Figure 3A through 3C). Images of histological morphology (Figure 3D through 3F) are in agreement with this scenario. The accumulation of interstitial lipid droplets, which can be viewed in CARS imaging (Figure 3A, 3H, and 3I), has not yet formed a confluent and well-defined lipid core within the thickened intima (as compared to Type IV and V). The disordered collagen fibrils around the lipid pools were detected (Figure 3B and 3H). The randomly distributed lipid droplets underscored the observation of a Type III lesion.

Compared with a Type III lesion, a Type IV lesion, as shown in Figure 4, consists of a well-defined lipid core which renders a strong CARS signal (intense, bright) starting from the shoulder region of the plaque (Figure 4A). Intimal

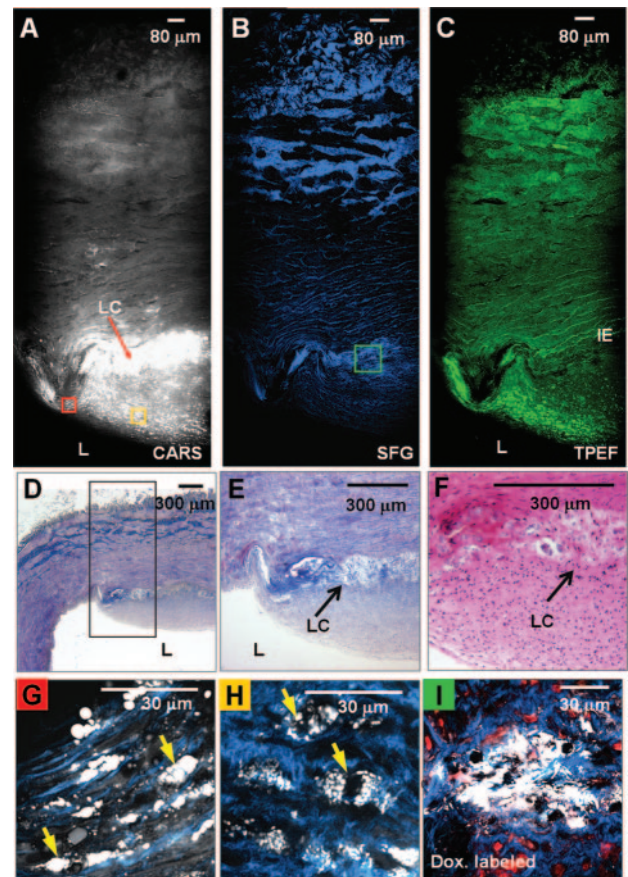


Figure 4. Representative images of a Type IV lesion inspected by CARS (A), SFG (B), and TPEF (C). The lipid core (LC) was identified by CARS. D and E, Masson trichrome staining. Black rectangle indicates the corresponding area in A through C. F, H&E staining. G and H, Colocalized NLO images corresponding to the red and yellow squares in A, respectively. I, Doxorubicin-labeled (red) image, around lipid core, colocalized with CARS and SFG signals.

disorganization is obvious in the images (Figure 4A through 4C). The lesion episodes and fibril distributions viewed in the NLO images are confirmed by Masson trichrome (Figure 4D and 4E) and H&E staining (Figure 4F). Furthermore, the predominant cellular milieu with abundant foam cells can be viewed at the shoulder (Figure 4A and 4G) and around the luminal regions of the atherosclerotic plaque (Figure 4A and 4H). The foam cells appeared much more circular and densely packed with lipid at this stage (arrows). Doxorubicin labeling (Figure 4I), which is specific to nuclei, highlights the extracellular lipid accumulation within the lipid core viewed by CARS.

Figure 5 shows a typical type V (or Va) lesion. The dense core of lipid and necrotic debris accumulation viewed by CARS (Figure 5A) and the surrounding collagen fibrous cap imaged by SFG (Figure 5B), together with stronger auto-fluorescence viewed by TPEF in the core area (Figure 5C), illustrate a Type V lesion.^{35,36} The NLO imaging result is consistent with histology analyses of serial sections shown in Figure 5D through 5F. The surrounded collagen cap identified by the Masson trichrome staining (Figure 5D and 5E) and the light-microscope features of lipid gruel,⁴³ which give

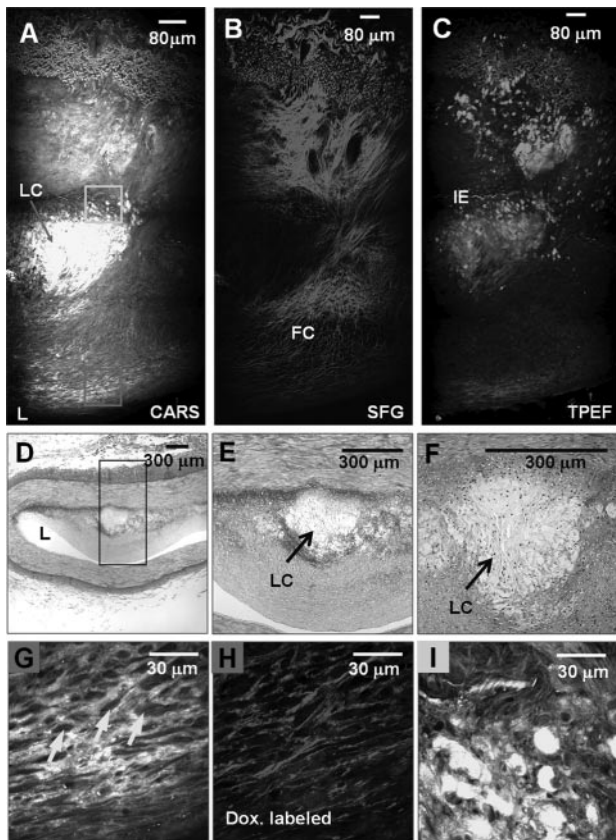


Figure 5. Representative images of a Type V lesion inspected by CARS (A), SFG (B), and TPEF (C). FC indicates collagen fibrous cap around the lipid core (LC). D, Masson trichrome stained image. Black rectangle: the correlative area in A through C. E and F, Zoomed-in images of Masson trichrome and H&E staining around the lipid core. Colocalized NLO image in G and doxorubicin-labeled (red) image colocalized with SFG signal in H elucidate the relationship between elongated cells (arrows) and collagenous matrix. I, Colocalized NLO image from the yellow square in A.

the bubbly, granular, and anucleate necrotic debris (Figure 5E and 5F), highly support the NLO imaging results. The location of internal elastic lamina (Figure 5A and 5C) and cell organizations (Figure 5G and 5H) viewed in NLO images are in keeping with the histology observation. The lipid gruel inside the lipid core viewed by CARS (Figure 5I) suggests that the relatively higher TPEF signal in the core area (Figure 5C) probably arose from oxidized-LDL.

In a calcific atheroma classified as Type VII (or Vb),^{35,36} the intima-media interface is dominated by mineralization,

where no significant NLO signals were obtained (supplemental Figure II). A complex lesion milieu can be observed. Staining by the von Kossa method confirmed the calcification lesion.

Quantitative Analysis of Lipid and Collagen Contents in Different Lesion Types

It is established that CARS microscopy permits label-free quantitation of lipid droplets in cells and tissues.^{26,44} To validate the SFG signal, we performed a correlation study of collagen content measured by SFG and that by Masson trichrome staining and obtained a correlation coefficient of ≈ 0.75 (supplemental Figure III). Based on the CARS and SFG intensities, we have calculated the lipid and collagen contents in thickened intima of different lesions (see Materials and Methods). The quantitative results are summarized in the Table. As expected,⁴⁵ the area percentage of lipid deposition was lower in early-stage lesions than in advanced lesions. The Type IV lesion demonstrated the highest percentage of lipid accumulation ($>45\%$ of intima). The lower lipid deposition found in Types V and VII implies the likelihood of retrogression of lipid accumulation and the development of fibrous deposition and mineralization. With respect to collagen content, the type V lesion showed a higher area percentage of collagen ($>40\%$ of intima) than earlier stages. Notably, the type IV lesion with a necrotic core and a low degree of fibrosis formation^{33,35} showed a lower collagen-to-lipid ratio than early lesions.

Discussion

We have shown that CARS-based multimodal NLO microscopy is capable of viewing the various pathological components of atherosclerotic lesions and, as such, can act as an in situ histological tool that is free from the labeling requirement of conventional methods. Moreover, based on the CARS and SFG signal intensities, we were able to carry out a quantitative analysis of collagen and lipid deposition in intima of different lesions. Thus, NLO microscopy gives us both a morphological, as well as quantitative, tool by which to characterize lesions and the percentage contents of lipid and collagen, respectively. The importance of this capability arises from the fact that lipid and collagen contents dominate the formation of soft and hard tissues that affect the mechanical properties of atherosclerotic arteries.^{46,47} In this context, our results show the potential of NLO microscopy in provid-

Table. Lipid and Collagen Percentage Within Thickened/Pathological Intima

Lesion Type	n	Lipid %	Collagen %	Collagen/Lipid Ratio
Type I Initial lesion	3	2.08 \pm 1.21	14.20 \pm 9.41	6.78 \pm 4.39
Type II Fatty streak	3	9.60 \pm 3.39	20.44 \pm 5.19	2.35 \pm 0.98
Type III Intermediate lesion	2	27.78 \pm 7.50	28.50 \pm 7.56	0.98 \pm 0.10
Type IV Atheroma	4	48.69 \pm 6.79	35.84 \pm 2.98	0.74 \pm 0.08
Type V Fibrous atheroma	2	27.20 \pm 4.28	44.00 \pm 0.70	1.64 \pm 0.23
Type VII Calcific atheroma	1	9.48	31.94	3.37

Data are mean \pm SD ($P<0.01$). n indicates number of lesions.

Significant differences were observed in lipid percentage between type IV and other types ($P<0.05$).

Significant differences were observed in collagen percentage between type V and others ($P<0.05$).

ing microenvironmental information for mechanical modeling of atherosclerosis.

In this study, we manually stitched images at the most severe location of each lesion because of the limited field of view of NLO microscopy. Imaging the whole cross-section will be very helpful to identify lesions and for quantitative studies. This technical challenge can be overcome by combining laser-scanning with sample scanning on a stepping motor stage.^{48–50} Photodamage effects in a femtosecond NLO system⁵¹ were not observed in our CARS-based NLO system. Instead of femtosecond pulse excitation, we used 2.5-ps lasers at 707 nm and 884 nm with 40 mW and 20 mW at sample, respectively. At constant damaging potential, it was demonstrated that signals may even be larger with ps pulses because the exponent of the power law of damage is higher than that of the signal.⁵²

Lilledahl and colleagues recently demonstrated that SHG and TPEF imaging of fibrous caps can be used for identifying vulnerable plaques.⁵¹ The vulnerability and tendency to rupture, however, depend not only on the fibrous cap thickness, but also on its superimposition with other complex factors, such as accumulation of lipid and macrophage foam cells, infiltration of inflammatory cells, and secretion of collagen degradation factors.^{53,54} By adding the capability of viewing foam cells and lipid deposition, CARS-based multimodal NLO imaging provides a significant improvement for mapping the superficial area of a plaque and assessing its vulnerability to rupture and exposure of the lipid core. Luminal scanning of subendothelial scenario (supplemental Figure IV) could potentially be used for assessing instability or vulnerability. In this work, however, such imaging was restricted by the penetration depth of around 60 μm . Nonetheless, with adaptive optics,⁵⁵ microprobe objective,⁵⁶ or longer excitation wavelength,²⁵ the imaging depth could be remarkably increased to hundreds of microns. Because the empirical definition of plaque cap was 60 to 65 μm in unstable lesion^{43,45,57} and about 25 to 35 μm in disrupted coronary arteries,^{43,45,58} the improved penetration depth is expected to meet the need for vulnerability studies.

Toward the goal of intravital NLO biopsy, multiphoton fluorescence endoscopy has been reported.^{59,60} It is also notable that SHG contrast-enhanced OCT is emerging for in situ cross-sectional imaging.^{61–63} More recently, the preliminary concept of CARS endoscopy has been proposed.⁶⁴ An advantage of CARS and SHG imaging is that tissues are not required to undergo slicing, paraffin embedding, or freeze-thaw processes, thus maintaining the potential of intravital imaging. With the capability of quantifying lipid body and collagen fibril contents as shown in the present study, it is foreseeable that a multimodal NLO intravascular catheter with miniaturized probing devices could facilitate and benefit in vivo studies and diagnosis in the years to come.

Acknowledgments

The authors cordially thank Thuc Le for the insightful discussion.

Sources of Funding

This work was supported by a NIH R01 grant EB007243 to Cheng, NIH grants RR013223 and HL062552 to Sturek, and the Comparative Medicine Program.

Disclosures

None.

References

1. AHA. Heart Disease and Stroke Statistics - 2008 update. 2008.
2. Yusuf S, Reddy S, Ounpuu S, Anand S. Global burden of cardiovascular diseases part I: general considerations, the epidemiologic transition, risk factors and impact of urbanization. *Circulation*. 2001;104:2746–2753.
3. Sanz J, Fayad ZA. Imaging of atherosclerotic cardiovascular disease. *Nature*. 2008;451:953–957.
4. Nahrendorf M, Jaffer FA, Kelly KA, Sosnovik DE, Aikawa E, Libby P, Weissleder R. Noninvasive Vascular Cell Adhesion Molecule-1 Imaging Identifies Inflammatory Activation of Cells in Atherosclerosis. *Circulation*. 2006;114:1504–1511.
5. Amirbekian V, Lipinski MJ, Briley-Saebo KC, Amirbekian S, Aguinaldo JGS, Weinreb DB, Vucic E, Frias JC, Hyafil F, Mani V, Fisher EA, Fayad ZA. Detecting and assessing macrophages in vivo to evaluate atherosclerosis noninvasively using molecular MRI. *Proc Natl Acad Sci U S A*. 2007;104:961–966.
6. Moore M, Spencer T, Salter D, Kearney P, Shaw T, Starkey I, Fitzgerald P, Erbel R, Lange A, McDicken N, Sutherland G, Fox K. Characterisation of coronary atherosclerotic morphology by spectral analysis of radiofrequency signal: in vitro intravascular ultrasound study with histological and radiological validation. *Heart*. 1998;79:459–467.
7. Nair A, Kuban BD, Obuchowski N, Vince DG. Assessing spectral algorithms to predict atherosclerotic plaque composition with normalized and raw intravascular ultrasound data. *Ultrasound Med Biol*. 2001;27:1319–1331.
8. Kenya N, Etsuo T, Osamu K, Vince DG, Renu V, Jean-Francois S, Akira M, Yoshihiro T, Tatsuya I, Mariko E, Tetsuo M, Mitsuyasu T, Takahiko S. Accuracy of In Vivo Coronary Plaque Morphology Assessment: A Validation Study of In Vivo Virtual Histology Compared With In Vitro Histopathology. *J Am Coll Cardiol*. 2006;47:2405–2412.
9. Megens RTA, Reitsma S, Schiffers PHM, Hilgers RHP, De Mey JGR, Slaaf DW, oude Egbrink MGA, van Zandvoort MAMJ. Two-Photon Microscopy of Vital Murine Elastic and Muscular Arteries. *J Vasc Res*. 2007;44:87–98.
10. Yu W, Braz JC, Dutton AM, Prusakov P, Rekhter M. In vivo imaging of atherosclerotic plaques in apolipoprotein E deficient mice using nonlinear microscopy. *J Biomed Optics*. 2007;12:054008.
11. Zipfel WR, Williams RM, Webb WW. Nonlinear magic: multiphoton microscopy in the biosciences. *Nat Biotech*. 2003;21:1369–1377.
12. Helmchen F, Denk W. Deep tissue two-photon microscopy. *Nat Meth*. 2005;2:932–940.
13. Zipfel WR, Williams RM, Christie R, Nikitin AY, Hyman BT, Webb WW. Live tissue intrinsic emission microscopy using multiphoton-excited native fluorescence and second harmonic generation. *Proc Natl Acad Sci U S A*. 2003;100:7075–7080.
14. Shen YR. Surface properties probed by SHG and SFG. *Nature*. 1989;337:519–525.
15. Moreaux L, Sandre O, Mertz J. Membrane imaging by second-harmonic generation microscopy. *J Opt Soc Am B*. 2000;17:1685–1694.
16. Campagnola PJ, Loew LM. Second-harmonic imaging microscopy for visualizing biomolecular arrays in cells, tissues and organisms. *Nat Biotech*. 2003;21:1356–1360.
17. Williams RM, Zipfel WR, Webb WW. Interpreting SHG images of collagen I fibrils. *Biophys J*. 2005;88:1377–1386.
18. Fu Y, Wang H, Shi R, Cheng JX. Second harmonic and sum frequency generation imaging of fibrous astroglial filaments in ex vivo spinal tissues. *Biophys J*. 2007;92:3251–3259.
19. Zoumi A, Yeh A, Tromberg BJ. Imaging cells and extracellular matrix in vivo by using SHG and TPEF. *Proc Natl Acad Sci U S A*. 2002;99:11014–11019.
20. Barad Y, Eisenberg H, Horowitz M, Silberberg Y. Nonlinear scanning laser microscopy by third harmonic generation. *Appl Phys Lett*. 1997;70:922–924.
21. Debarre D, Supatto W, Pena A-M, Fabre A, Tordjmann T, Combettes L, Schanne-Klein M-C, Beaupaire E. Imaging lipid bodies in cells and tissues using third-harmonic generation microscopy. *Nat Meth*. 2006;3:47–53.
22. Cheng JX, Xie XS. Coherent anti-Stokes Raman scattering microscopy: instrumentation, theory, and applications. *J Phys Chem B*. 2004;108:827–840.

23. Cheng JX Coherent anti-stokes Raman scattering microscopy. *Appl Spectroscopy*. 2007;61:197A–208A.
24. Wang H, Fu Y, Zickmund P, Shi R, Cheng JX. Coherent anti-stokes Raman scattering imaging of axonl myelin in live spinal tissues. *Biophys J*. 2005;89:581–591.
25. Evans CL, Potma EO, Puoris'haag M, Côté D, Lin CP, Xie XS. Chemical imaging of tissue *in vivo* with video-rate coherent anti-Stokes Raman scattering microscopy. *Proc Natl Acad Sci U S A*. 2005;102:16807–16812.
26. Nan X, Cheng J-X, Xie XS. Vibrational imaging of lipid droplets in live fibroblast cells with coherent anti-Stokes Raman scattering microscopy. *J Lipid Res*. 2003;44:2202–2208.
27. Li L, Wang H, Cheng J-X. Quantitative coherent anti-stokes Raman scattering imaging of lipid distribution in coexisting domain. *Biophys J*. 2005;89:3480–3490.
28. Zoumi A, Lu X, Kassab GS, Tromberg BJ. Imaging coronary artery microstructure using SHG and TPEF. *Biophys J*. 2004;87:2778–2786.
29. Zandvoort M, Engels W, Douma K, Beckers L, Egbrink M, Daemen M, Slaaf DW. TP microscopy for imaging of the vascular wall: a proof of concept study. *J Vasc Res*. 2004;41:54–63.
30. Douma K, Megens RTA, Reitsma S, Prinzen L, Slaaf DW, Zandvoort M. Two-photon lifetime imaging of fluorescent probes in intact blood vessels: A window to sub-cellular structural information and binding status. *Microsc Res Tech*. 2007;70:467–475.
31. Le TT, Langohr IM, Locker MJ, Sturek M, Cheng JX Label-free molecular imaging of atherosclerotic lesions using multimodal nonlinear optical microscopy. *J Biomed Opt*. 2007;12:0540071–05400710.
32. Wang HW, Le TT, Cheng JX. Label-free imaging of arterial cells and extracellular matrix using a multimodal nonlinear optical microscope. *Opt Comm*. 2008;281:1813–1822.
33. Virmani R, Kolodgie FD, Burke AP, Farb A, Schwartz SM. Lessons from sudden coronary death: A comprehensive morphological classification scheme for atherosclerotic lesions. *Arterioscler Thromb Vasc Biol*. 2000; 20:1262–1275.
34. Stary HC, Chandler AB, Dinsmore RE, Fuster V, Glagov S, Insull W Jr, Rosenfeld ME, Schwartz CJ, Wagner WD, Wissler RW. A definition of initial, fatty streak, and intermediate lesions of atherosclerosis: A Report From the Committee on Vascular Lesions of the Council on Arteriosclerosis, AHA. *Circulation*. 1994;14:840–856.
35. Stary HC, Chandler AB, Dinsmore RE, Fuster V, Glagov S, Insull W Jr, Rosenfeld ME, Schwartz CJ, Wagner WD, Wissler RW. A definition of advanced types of atherosclerotic lesions and a histological classification of atherosclerosis: A Report From the Committee on Vascular Lesions of the Council on Arteriosclerosis, AHA. *Circulation*. 1995;92:1355–1374.
36. Stary HC. Natural history and histological classification of atherosclerotic lesions: An update. *Arterioscler Thromb Vasc Biol*. 2000;20:1177–1178.
37. Sturek M, Alloosh M, Wenzel J, Byrd JP, Edwards JM, Lloyd PG, Tune JD, March KL, Miller MA, Mokolke EA, Brisbin IL. Ossabaw Island miniature swine: cardiometabolic syndrome assessment. In Swindle MM. *Swine in the Laboratory: Surgery, Anesthesia, Imaging, and Experimental Technique*. Boca Raton: CRC Press; 2007.
38. Dyson M, Alloosh M, Vuchetich J, Mokolke E, Sturek M. Components of metabolic syndrome and coronary artery disease in female Ossabaw swine fed excess atherogenic diet. *Comp Med*. 2006;56:35–45.
39. Andreeva ER, Pugach IM, Orekhov AN. Collagen-synthesizing cells in initial and advanced atherosclerotic lesions of human aorta. *Atherosclerosis*. 1997;130:133–142.
40. Lorenz MW, Markus HS, Bots ML, Rosvall M, Sitzer M. Prediction of clinical cardiovascular events with carotid intima-media thickness: a systematic review and meta-analysis. *Circulation*. 2007;115:459–467.
41. Arakawa K, Isoda K, Ito T, Nakajima K, Shibuya T, Ohsuzu F. Fluorescence analysis of biochemical constituents identifies atherosclerotic plaque with a thin fibrous cap. *Arterioscler Thromb Vasc Biol*. 2002;22: 1002–1007.
42. Meyer JW, Schmitt ME. A central role for the endothelial NADPH oxidase in atherosclerosis. *FEBS Lett*. 2000;472:1–4.
43. Moreno PR, Purushothaman KR, Fuster V, O'Connor WN. Intimomedial interface damage and adventitial inflammation is increased beneath disrupted atherosclerosis in the aorta: Implications for plaque vulnerability. *Circulation*. 2002;105:2504–2511.
44. Hellerer T, Axang C, Brackmann C, Hillertz P, Pilon M, Enejder A. Monitoring of lipid storage in *Caenorhabditis elegans* using coherent anti-Stokes Raman scattering microscopy. *Proc Natl Acad Sci U S A*. 2007;104:14658–14663.
45. Virmani R, Burke AP, Farb A, Kolodgie FD. Pathology of the vulnerable plaque. *J Am Coll Cardiol*. 2006;47:C13–18.
46. Dugnani R, Chang FK. In vitro atherosclerotic plaque characterization by acoustic impedance monitoring, part I: sensor modeling, design, and fabrication. *Journal of Intelligent Material Systems and Structures*. 2008; 19:815–826.
47. Lee RT, Grodzinsky AJ, Frank EH, Kamm RD, Schoen FJ. Structure-dependent dynamic mechanical behavior of fibrous caps from human atherosclerotic plaques. *Circulation*. 1991;83:1764–1770.
48. Chow SK, Hakoziaki H, Price DL, Maclean NAB, Deerinc TJ, Bouwer JC, Martone ME, Peltier ST, Ellisman MH. Automated microscopy system for mosaic acquisition and processing. *J Microsc*. 2006;222: 76–84.
49. Evans CL, Xu X, Kesari S, Xie XS, Wong STC, Young GS. Chemically-selective imaging of brain structures with CARS microscopy. *Opt Express*. 2007;15:12076–12087.
50. Fu Y, Huff TB, Wang H-W, Cheng J-X, Wang H. Ex vivo and in vivo imaging of myelin fibers in mouse brain by coherent anti-Stokes Raman scattering microscopy. *Optics Express*. 2008;16:19396–19409.
51. Lilledahl MB, Haugen OA, Davies CdL, Svaasand LO. Characterization of vulnerable plaques by multiphoton microscopy. *J Biomed Opt*. 12:044005–044012, 2007.
52. Hopt A, Neher E. Highly nonlinear photodamage in two-photon fluorescence microscopy. *Biophys J*. 2001;80:2029–2036.
53. Moreno PR, Falk E, Palacios IF, Newell JB, Fuster V, Fallon JT. Macrophage infiltration in acute coronary syndromes. Implications for plaque rupture. *Circulation*. 1994;90:775–778.
54. Libby P, Aikawa M. Stabilization of atherosclerotic plaques: New mechanisms and clinical targets. *Nat Med*. 2002;8:1257–1262.
55. Wright AJ, Poland SP, Girkin JM, Freudiger CW, Evans CL, Xie XS. Adaptive optics for enhanced signal in CARS microscopy. *Opt Express*. 2007;15:18209–18219.
56. Wang H, Huff TB, Fu Y, Jia KY, Cheng J-X. Increasing the imaging depth of coherent anti-Stokes Raman scattering microscopy with a miniature microscope objective. *Opt Lett*. 2007;32:2212–2214.
57. Burke AP, Farb A, Malcom GT, Liang Y-h, Smialek J, Virmani R. Coronary risk factors and plaque morphology in men with coronary disease who died suddenly. *N Engl J Med*. 1997;336:1276–1282.
58. Moreno PR, Purushothaman KR, Fuster V, Echeverri D, Trusczyńska H, Sharma SK, Badimon JJ, O'Connor WN. Plaque neovascularization is increased in ruptured atherosclerotic lesions of human aorta: implications for plaque vulnerability. *Circulation*. 2004;110:2032–2038.
59. Flusberg BA, Cocker ED, Piyawattanametha W, Jung JC, Cheung ELM, Schnitzer MJ. Fiber-optic fluorescence imaging. *Nat Meth*. 2005;2: 941–950.
60. Fu L, Gu M. Fibre-optic nonlinear optical microscopy and endoscopy. *J Microsc*. 2007;226:195–206.
61. Tang S, Sun C-H, Krasieva TB, Chen Z, Tromberg BJ. Imaging sub-cellular scattering contrast by using combined optical coherence and multiphoton. *Opt Lett*. 2007;32:503–505.
62. Bredfeldt JS, Vinegoni C, Marks DL, Boppart SA. Molecularly sensitive optical coherence tomography. *Opt Lett*. 2005;30:495–497.
63. Su J, Tomov IV, Jiang Y, Chen Z. High-resolution frequency-domain second-harmonic optical coherence tomography. *Applied Optics*. 2007; 46:1770–1775.
64. Légaré F, Evans CL, Ganikhanov F, Xie XS. Towards CARS endoscopy. *Opt Express*. 2006;14:4427–4432.